university of groningen

faculty of science and engineering

Investigation of trigger lines in view of a search for lepton-flavor violating in $\Lambda_b \to \Lambda\tau\mu$ decay

Author:
Kevin MARTINEZ DAMIATI
(s5291089)

Supervisor:
Dr. Ann-Kathrin PERREVOORT
Second examiner :
Dr. Daan VAN EIJK

Bachelor's Thesis
To fulfill the requirements for the degree of
Bachelor of Science in Physics
at the University of Groningen

July 11, 2025

Contents

Page

Abstract **3**

Acknowledgements **4**

1 Introduction **5**

2 Theoretical Background **7**
2.1 The Standard Model 7
2.2 Lepton Flavor Violation 8
2.3 The Decay Process: $\Lambda_b \to \Lambda \tau^{\pm} \mu^{\mp}$ 8

3 Methodology **11**
3.1 The LHCb Detector 11
3.1.1 Trigger System 12
3.2 Simulation Environment 14

4 Results **17**
4.1 $\Lambda_b \to \Lambda \tau^{\mp} \mu^{\pm}$ 17
4.1.1 Long–Long Track Configuration 17
4.1.2 Downstream–Downstream Track Configuration 19
4.2 $\Lambda_b \to \Lambda \tau^{\mp} \tau^{\pm}$ 21
4.2.1 Long–Long Track Configuration 21
4.2.2 Downstream–Downstream Track Configuration 23

5 Discussion **27**

6 Conclusion **30**

Bibliography **32**

Abstract

This study investigates the trigger efficiency for the rare lepton-flavour violating decay $\Lambda_b \to \Lambda \tau^{\mp} \mu^{\pm}$ at the LHCb experiment, to evaluate the performance of existing trigger lines and identify areas for optimization. Simulated signal events were generated using RapidSim, alongside a background decay mode, $\Lambda_b \to \Lambda \tau^{\pm} \tau^{\mp}$, which shares the same final-state topology. A detailed analysis was performed by varying the transverse momentum (p_T) thresholds for individual particles and assessing their impact on trigger selection. The pion daughter of Λ had the most significant effect on efficiency, with cuts above 1 GeV leading to plateaued performance. The proton and muon selections were found to be less restrictive, and tightening the muon selection offered the most potential for optimization. Trigger efficiency comparisons showed that DD tracks, which bypass the VELO, achieved trigger efficiencies of $33.4 \pm 0.5\%$ and $25.2 \pm 0.5\%$ for the signal and background decays, respectively, whereas LL tracks yielded $20.7 \pm 0.8\%$ and $13.7 \pm 0.8\%$. The former configuration sacrifices vertex precision for higher trigger acceptance. Nevertheless, the overall decay reconstruction efficiency ranged between $3.4 \pm 0.1\%$ and $6.0 \pm 0.3\%$, highlighting a need for more inclusive trigger designs. These findings suggest that dedicated trigger lines and refined particle selection criteria, particularly for the muon and pion, could significantly enhance signal sensitivity. Future work should incorporate full detector simulation to validate these results and inform the design of more effective trigger strategies for rare decay searches.

Acknowledgments

I would like to express my sincere gratitude to my supervisor, Dr. Ann-Kathrin Perrevoort, for her invaluable guidance and support throughout this thesis. Her prompt responses, clear explanations, and insightful suggestions were instrumental in helping me understand this topic.

Non nobis, Domine, non nobis, sed nomini tuo da gloriam.

1 Introduction

The beginning of the Universe, as currently understood, started with the Big Bang. Time, space, and matter emerged from an extremely hot and dense initial state. Although the exact conditions preceding this event are not yet known, the subsequent expansion is believed to have produced matter and antimatter in nearly equal quantities. However, a small excess of matter over antimatter developed, a phenomenon known as the baryon asymmetry of the Universe (BAU) [1]. The origin of this imbalance remains one of the most fundamental open questions in modern physics, suggesting the existence of processes beyond the Standard Model (SM) of particle physics, particularly new sources of Charge-Parity (CP) violation. This requirement arises from the Sakharov conditions, which state that three conditions must be satisfied to generate a baryon asymmetry: baryon number (B) violation, Charge (C) and CP violation, and departure from thermal equilibrium [2].

CP violation was first observed in the 1960s in neutral kaon decays, but the amount allowed by the SM, primarily within the quark sector, is insufficient to account for the observed BAU [1]. As a result, certain beyond the Standard Model (BSM) frameworks, such as the seesaw mechanism, which incorporates neutrino masses, allow for CP violation to occur in the lepton sector. If neutrinos are Majorana particles, that is, they are their own antiparticles, additional CP-violating phases may appear. These could be visible in neutrino oscillation experiments as differences in the behavior of neutrinos and antineutrinos, indicating leptonic CP violation. The discovery of neutrino oscillations has already confirmed that neutrinos have mass, a fact that contradicts SM predictions, further motivating such extended models [2, 3].

Although CP violation in mesons have been extensively measured, evidence for CP violation in baryons remains scarce, despite baryonic matter forming the dominant component of visible matter in the Universe. A recent study by the LHCb collaboration reported the first evidence of CP violation in baryons, observed in Λ_b decays [4]. However, the statistical precision of this result remains limited, and further investigation is necessary to confirm and comprehend the dynamics involved.

To explain the BAU, many theoretical models propose not only new sources of CP violation but also mechanisms that violate lepton flavor conservation. Although lepton flavor violation (LFV) is strictly forbidden in the SM for charged leptons, it occurs naturally in many BSM scenarios, especially those involving massive neutrinos. This has motivated the search for rare LFV processes, which offer sensitive probes of the flavor structure of BSM models and may be closely linked to the same properties responsible for CP violation and the matter–antimatter imbalance [5].

One compelling framework that unites leptonic CP violation and LFV to the BAU is leptogenesis. In this scenario, CP-violating decays of heavy Majorana neutrinos in the early Universe generated a lepton asymmetry, which was then converted into a baryon asymmetry through electroweak sphaleron processes [2]. Experimental searches for LFV decays, such as those conducted at the LHCb experiment, therefore, offer a unique opportunity to test the flavor and CP-violating mechanisms predicted by these BSM theories.

A particularly interesting channel in this context is the rare baryonic decay $\Lambda_b \to \Lambda \tau \mu$, which is forbidden in the SM under the assumption of lepton flavor conservation [6]. Although LFV has been studied extensively in mesonic decays, baryonic LFV channels remain underexplored, offering a complementary perspective on potential BSM interactions, such as those involving leptoquarks or heavy

neutral gauge bosons [4]. Furthermore, the presence of a tau lepton in the final state adds significant experimental challenges due to its short lifetime, multiple decay modes, both hadronic and leptonic, and the presence of undetectable neutrinos in all its decays, which complicate detection and kinematic reconstruction. [7, 8].

Consequently, this decay is currently under investigation at the LHCb experiment at CERN, which is specifically designed for high-precision studies of b- and c-hadron decays. With its forward geometry and advanced trigger system, LHCb is particularly well-suited for investigating rare decays and testing the boundaries of the Standard Model. However, due to the high collision rate at the LHC, only a small subset of events can be stored for offline analysis. The LHCb trigger system thus plays a crucial role in selecting events of interest by applying real-time criteria [9]. In this context, the presence of a muon in the final state is particularly advantageous, as it can be efficiently identified using the dedicated muon chambers, enhancing the likelihood that such events are retained by the trigger [10].

This thesis investigated the efficiency of the current trigger lines in selecting $\Lambda_b \to \Lambda \tau \mu$ decays, using simulated data generated with the Monte Carlo tool RapidSim [11]. This tool enables the creation of large samples of signal events with realistic kinematics adapted to the LHCb environment. The aim was to evaluate how effectively the existing trigger configuration captures this LFV channel and to identify potential areas for improvement. This was achieved by applying the kinematic cuts defined by the trigger system to the simulated sample and comparing the number of selected events to the total. Based on this analysis, it becomes possible to determine which constraints may be optimized to enhance the detectability of this rare decay.

2 Theoretical Background

2.1 The Standard Model

The Standard Model (SM) is a theoretical framework developed in the latter half of the 20th century that describes three of the four known fundamental forces: the electromagnetic, weak, and strong nuclear interactions. Gravity, however, remains outside its scope and is instead described separately by general relativity. Despite this limitation, the SM has been extensively tested and confirmed through experiments, most notably with the discovery of the Higgs boson in 2012 at CERN, which provided the last missing piece of the model [12].

According to the SM, all known matter is composed of elementary particles called fermions, which are considered indivisible. These particles are classified into two main families: quarks and leptons, as shown in Figure 1. Each group consists of six particles, organized into three generations. The first generation contains the lightest and most stable particles, which make up all ordinary matter, while particles from the second and third generations are unstable and decay rapidly into their lighter counterparts. The six quarks are grouped into three generations: up (u) and down (d); charm (c) and strange (s); and top (t) and bottom (b). Quarks possess a property known as color charge, which is associated with the strong interaction. They combine in such a way that all observable particles, such as protons and neutrons, are color neutral, a phenomenon governed by quantum chromodynamics (QCD), the theory of the strong interaction within the SM. Additionally, quarks combine to form hadrons, which are classified as baryons, composed of three quarks, and mesons, composed of a quark and an anti-quark. Analogously, there are six leptons arranged in three generations: the charged leptons, the electron (e), the muon (μ), and the tau (τ), along with their corresponding neutrinos, ν_e, ν_μ, and ν_τ. Charged leptons carry electric charge and have a measurable mass, while neutrinos are electrically neutral and possess extremely small masses [13].

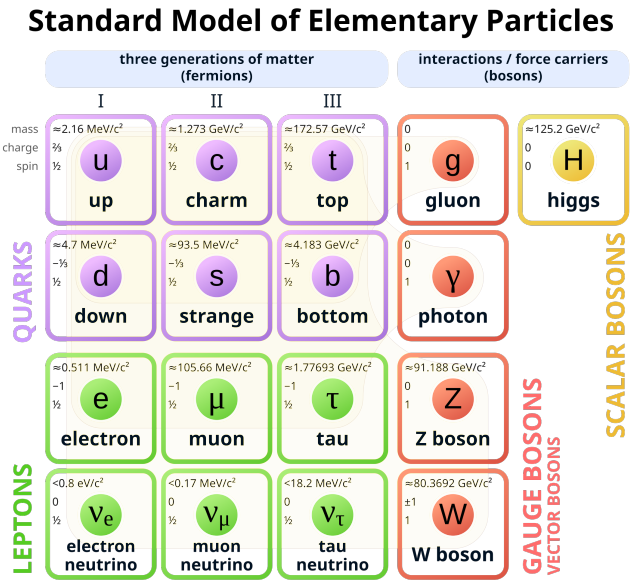

Figure 1: The elementary particles of the Standard Model, categorized by type and key quantum properties [14].

Additionally, the fundamental forces in the SM are mediated by gauge bosons, which are force-

carrying particles responsible for transmitting these interactions. There are four types of gauge bosons within the SM: photons, γ, which mediate the electromagnetic force; $W^{\pm}$ and Z^0 bosons, responsible for the weak force; and gluons, g, which mediate the strong force [13].

2.2 Lepton Flavor Violation

Lepton flavor violation (LFV) refers to processes in which a lepton of one flavor, such as a tau, converts into a lepton of another flavor, such as a muon, thereby violating conservation of individual lepton family numbers (L_e, L_μ, L_τ) [15]. Although neutrino oscillations confirm LFV in the neutral lepton sector, they induce LFV in charged lepton processes only via loop diagrams at rates that are extremely small, typically with predicted branching fractions on the order of $O(10^{-54})$ [5].

A key prediction of the SM is the strict conservation of individual lepton flavors for all leptons. This means that processes such as $\mu \to e\gamma$, $\tau \to \mu\gamma$, and the baryonic decay $\Lambda_b \to \Lambda\tau\mu$, are forbidden in the SM at tree level due to the absence of lepton-flavor changing couplings in its Lagrangian [15]. However, the discovery of neutrino oscillations, where neutrinos change flavor as they propagate, demonstrated that neutrinos must have non-zero mass, implying that lepton flavor is not an exact symmetry of nature in the neutral lepton sector. This phenomenon is described by the Pontecorvo-Maki-Nakagawa-Sakata (PMNS) matrix, which mixes neutrino flavor and mass eigenstates [16]. As neutrino oscillations are far below current experimental sensitivity, any observation of LFV in charged leptons is a clear sign of physics beyond the Standard Model (BSM).

Several BSM scenarios predict enhanced LFV rates that could be accessible to current or near-future experiments. These include models with heavy right-handed neutrinos (as in the seesaw mechanism), supersymmetry (SUSY), leptoquarks (LQ), and extended gauge symmetries such as a new Z' boson [15, 17]. Unlike the minimal contribution from neutrino mixing, which yields branching ratios far below experimental sensitivity, these models introduce new particles or interactions that can mediate LFV through flavor-changing neutral currents (FCNCs), in which the quark flavor changes without swapping its charge, either at loop level or even at tree level [18]. Observable LFV would therefore signal new physics beyond the Standard Model and the effects of neutrino oscillations alone. Moreover, such mechanisms are often connected to other open questions in particle physics, including the matter-antimatter asymmetry and the nature of dark matter, which remain unexplained by the SM.

2.3 The Decay Process: $\Lambda_b \to \Lambda\tau^{\pm}\mu^{\mp}$

The decay $\Lambda_b \to \Lambda\tau\mu$ is a baryonic LFV process involving a transition between second- and third-generation leptons, in which the Λ_b baryon decays into a Λ baryon and a dilepton pair, $\tau^{\pm}$ and $\mu^{\mp}$. As such, it is a rare decay process that belongs to the broader class of $b \to s\,\ell^+\,\ell^-$ FCNC transitions. These transitions are mediated by the weak interaction but are forbidden at tree level in the SM and can only occur via higher-order loop diagrams involving hypothetical particles like the leptoquark, as shown in Figure 2, or heavy gauge bosons (e.g., Z'), which provide the necessary flavor-violating couplings [18]. In this case, the $b \to s$ quark transition is accompanied by the emission of a τ and a μ, thereby violating lepton flavor universality and resulting in a strong suppression within the SM. However, when using new physics operators, the predicted branching fractions becomes $O(10^{-9})$ for

related decays such as $\Lambda_b \to \Lambda e\mu$ [19].

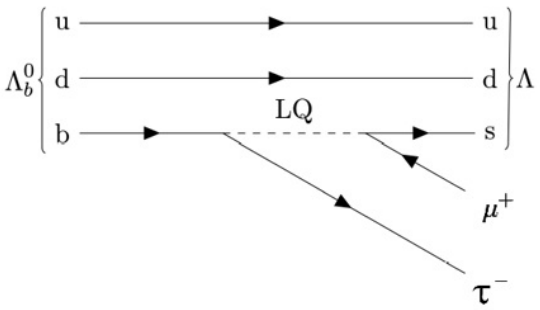

Figure 2: Adaptation of a Feynman diagram from Greeven illustrating the $\Lambda_b \to \Lambda\tau\mu$ mediated by a hypothetical leptoquark (LQ) [18].

Compared to mesonic $b \to s\ell^+\ell^-$ decays, baryonic modes such as $\Lambda_b \to \Lambda\ell^+\ell^-$ exhibit enhanced decay rates in the high-q^2 region due to differences in hadronic form factors and the richer spin structure of baryons [18]. This distinction provides a complementary kinematic region to probe potential BSM effects.

Since the Λ baryon predominantly decays via the weak interaction, it transforms into a proton and a negatively charged pion, $\Lambda \to p\pi^-$. This two-body decay results from the transformation of the strange quark into an up quark mediated by a virtual W^- boson and is the most common and energetically favored decay channel, conserving all relevant quantum numbers as shown in Figure 3a. An overview of the properties of the particles involved can be seen in Table 1.

Particle	**Symbol**	**Quark Content**	**Mass (MeV/c^2)**	**Charge (e)**	**Spin**	**Lifetime (s)**
Λ_b	Λ_b^0	udb	5619.60	0	$1/2$	1.470×10^{-12}
Λ^0	Λ^0	uds	1115.68	0	$1/2$	2.632×10^{-10}
τ^-	τ^-	–	1776.86	-1	$1/2$	2.903×10^{-13}
μ^-	μ^-	–	105.66	-1	$1/2$	2.197×10^{-6}
π^+	π^+	$u\bar{d}$	139.57	$+1$	0	2.603×10^{-8}
π^-	π^-	$d\bar{u}$	139.57	-1	0	2.603×10^{-8}
p (proton)	p	uud	938.27	$+1$	$1/2$	Stable

Table 1: Key particles involved in the $\Lambda_b \to \Lambda^0\tau^-\mu^+$ decay chain and subsequent τ^- decay into $\pi^-\pi^+\pi^-\nu_\tau$, including final-state particles from $\Lambda^0 \to p\pi^-$ [20].

Furthermore, the τ lepton, as the heaviest charged lepton, decays promptly via leptonic modes, including, $\tau^- \to e^-\bar{\nu}_e\nu_\tau$, $\tau \to \mu^-\bar{\nu}_\mu\nu_\tau$ and hadronic modes, particularly, the three-pion decay $\tau^- \to \pi^-\pi^-\pi^+\nu_\tau$ as presented in Figure 3b. This analysis focuses on the hadronic decay channel because the finite τ lifetime results in a detached decay vertex relative to the Λ baryon. Consequently, it facilitates the reconstruction of the τ vertex because the three pions originate from a common secondary vertex with significant displacement from the primary interaction point. Although this displacement enables efficient suppression of background events, the presence of undetectable neutrinos in the

decay chain complicates the full kinematic reconstruction, reducing invariant mass resolution and limiting the ability to distinguish the signal from background or to separate Λ_b decays from other b-hadron processes.

Lastly, the μ lepton offers a stable and distinctive signature, which significantly enhances triggering efficiency and particle identification within the LHCb detector's trigger system. The presence of a muon, combined with a hadronically decaying τ, enables the application of advanced vertexing and kinematic fitting techniques, thereby improving the suppression of background contamination and increasing the overall signal sensitivity [21].

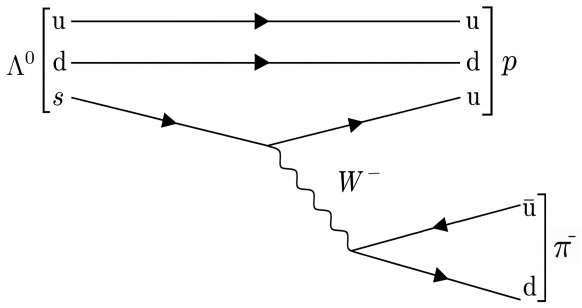

(a) Feynman diagram illustrating the decay of the Λ^0 baryon into a π^- and a proton, p, including the quark-level process mediated by the W^- boson via the weak interaction.

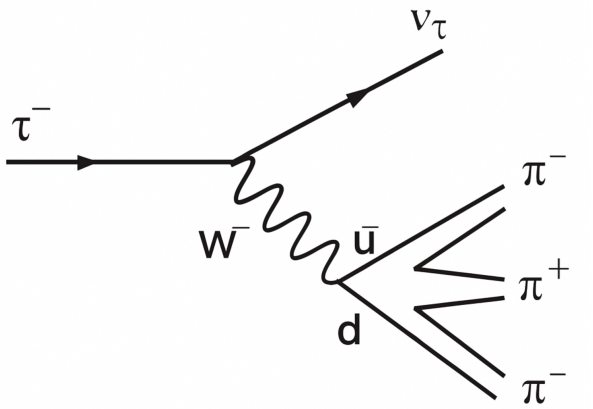

(b) Feynman diagram illustrating the decay of the τ^- lepton into two π^-, one π^+, and a neutrino ν_τ, mediated by the W^- boson via the weak interaction.

Figure 3: Sketches of two Feynman diagrams depicting the subdecays involved in the main decay process.

3 Methodology

3.1 The LHCb Detector

The Large Hadron Collider beauty (LHCb) experiment, shown in Figure 4, is a particle physics detector at the Large Hadron Collider (LHC) at CERN, specialized in measuring the parameters of CP violation, rare decays, lepton flavor violation, and other flavor-changing processes in the interactions of b- and c-hadrons, heavy particles containing bottom and charm quarks, to search for new physics. Its goal is to help understand the matter-antimatter asymmetry in the universe [22]. It is a single-arm forward spectrometer covering the pseudorapidity range $2 < \eta < 5$, which corresponds to very small angles (15–250 mrad) with respect to the beam direction. At these forward angles, in the center-of-mass (CM) frame, the b and $\bar{b}$ hadrons are produced predominantly back-to-back. However, due to the longitudinal boost of the CM system along the beam axis in the laboratory frame, both hadrons can appear in the same forward (or backward) region of the detector acceptance [18].

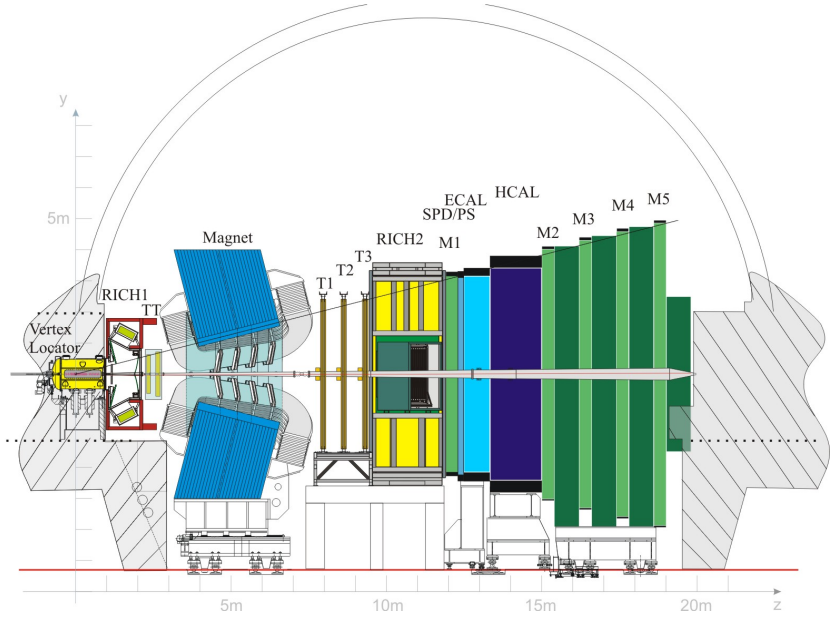

Figure 4: Schematic view of the LHCb detector along the bending plane, illustrating its main components for Run 1 and 2 [23].

The detector consists of several subsystems. Closest to the interaction region is the Vertex Locator (VELO), which provides high-precision tracking and vertex resolution, crucial for identifying displaced vertices from long-lived particles such as Λ_b [21]. In Runs 1 and 2, the VELO used silicon-strip sensors and was positioned approximately 8 mm from the primary vertex (PV) during stable beam conditions [23, 24].

Downstream of the VELO lies the tracking system, consisting of the Trigger Tracker (TT), placed upstream of a warm dipole magnet, and the tracking stations T1, T2, and T3 located downstream. This configuration enabled momentum reconstruction via the 4 Tm integrated magnetic field, whose polarity was periodically reversed to suppress detector-induced asymmetries. The tracking and VELO subsystems together allowed for the reconstruction of various track types, including VELO, upstream, long, and downstream tracks [23]. VELO tracks are reconstructed using hits solely within the VELO detector and provide precise measurements near the interaction point, essential for accurate vertex determination. Upstream tracks combine hits from the VELO and the TT stations but do not ex-

tend into the downstream trackers, allowing reconstruction of particles that do not traverse the full tracking system. Long tracks, which traverse the entire system, offer the most accurate momentum and vertex information, whereas downstream tracks originate beyond the VELO and are essential for reconstructing long-lived particles such as Λ^0. Therefore, particles considered in this analysis are required to decay within 2250 mm of the interaction point, corresponding to the longitudinal extent of the detector's active tracking region [21].

For particle identification, LHCb employs two Ring Imaging Cherenkov (RICH) detectors. These exploit the Cherenkov effect, where charged particles traveling through a medium faster than the local speed of light emit light at a characteristic angle. This angle depends on the velocity of the particles, and when combined with its momentum from tracking, allows its mass to be inferred [23]. In this way, the RICH system provides excellent π/p separation, which is essential for distinguishing between π and p, two charged hadrons with different masses that often appear in similar decay topologies [21].

The calorimeter system includes the Scintillating Pad Detector (SPD), a preshower detector (PS), the electromagnetic calorimeter (ECAL), and the hadronic calorimeter (HCAL). These subdetectors enable separation of electrons and photons, measure energy deposition from both electromagnetic and hadronic interactions, and provide fast signals for triggering. The muon system consists of five stations (M1–M5), designed to identify and track muons, key signatures in many rare decay modes, including the one studied in this thesis. Most stations use multi-wire proportional chambers (MWPCs), while triple-GEM detectors, gas electron multiplier detectors, are employed in the highest rate regions [23].

In preparation for Run 3, LHCb underwent a major upgrade to accommodate higher luminosity and enable full software-based triggering. The VELO was replaced with a silicon-pixel detector positioned closer to the beamline at 5.1 mm, improving spatial resolution and radiation hardness. The previous Trigger Tracker (TT) and T stations were replaced by the Upstream Tracker (UT), which provides precise momentum estimation before the magnet and aids in pattern recognition, and by a high-granularity Scintillating Fibre (SciFi) Tracker installed downstream of the magnet, improving overall tracking performance and radiation tolerance. Similarly, the RICH detectors were equipped with upgraded photodetectors and readout electronics to maintain PID performance under increased event rates. The calorimeter and muon systems retained their physical structures, but their readout electronics were enhanced to operate efficiently in the higher-luminosity Run 3 environment, i.e., the increased rate and data collection [25].

3.1.1 Trigger System

The LHCb experiment uses a two-stage trigger system to identify events of interest, such as those involving rare decays or long-lived particles, from approximately 40 million proton-proton collisions occurring every second. Due to the difficulty of storing all events, the trigger system rapidly filters them in multiple stages, ensuring that only relevant events are retained for further processing [21].

In Run 2, the first stage was the hardware trigger (L0), which relied on fast information from the calorimeter and muon systems. The hardware trigger reduced the event rate from approximately 40 million proton-proton collisions per second to about 1 million events per second, making the data stream manageable for software processing. In particular, the L0Muon trigger was charge symmetric,

meaning it did not distinguish between μ^+ and μ^-, thereby maintaining equal efficiency for both. This symmetry simplifies the analysis by allowing consideration of only one of the two opposite-sign lepton combinations.The second stage, the High-Level Trigger (HLT), performed a full software-based reconstruction of events, applying additional selection criteria such as kinematic cuts and particle identification. The HLT is typically divided into multiple stages that progressively refine the event selection using increasingly detailed algorithms, ensuring that rare and interesting physics signals, such as those involving long-lived particles or lepton flavor violation, are retained for further analysis [21]. A diagram of the LHCb Trigger Run 2 is shown in Figure 5.

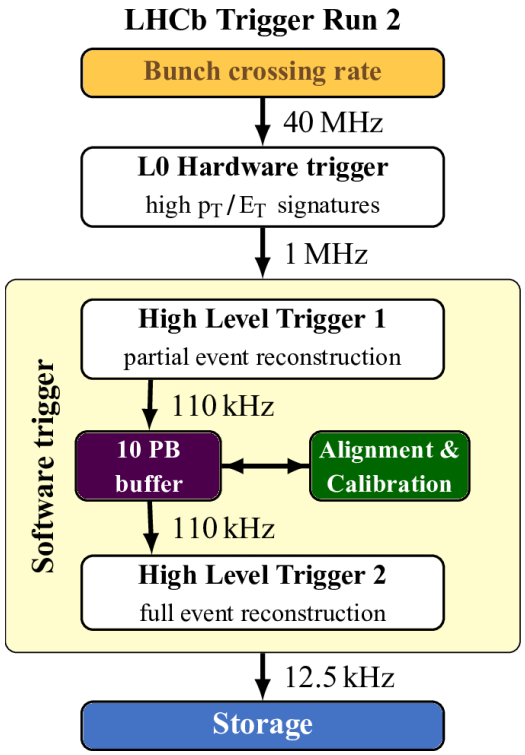

Figure 5: Diagram of the LHCb trigger system in Run 2 [24].

In Run 3, LHCb transitioned to a fully software-based trigger system, eliminating the hardware trigger stage. This upgrade allows the full detector data to be read out at the LHC bunch crossing rate of approximately 30 MHz, enabling more flexible and refined real-time event selection. The new architecture supports advanced real-time processing, including alignment, calibration, and improved particle identification, enhancing trigger efficiency, especially for low-momentum signatures and rare decay modes with complex final states [25].

To quantify the fraction of events that pass the trigger selection criteria implemented by the trigger system, the trigger efficiency is calculated using simulated events according to the following expression:

$$\varepsilon_{\text{trigger}} = \frac{N_{\text{selected}}}{N_{\text{generated}}} \tag{1}$$

where N_{selected} is the number of produced events that pass the geometric acceptance and the trigger selection requirements, and $N_{\text{generated}}$ is the total number of signal events produced in the simulation after passing the acceptance. This ratio provides an estimate of how many signal events the trigger is

capable of capturing under the given selection criteria.

Furthermore, the total selection efficiency for detecting and selecting a given event in the detector can be expressed as the product of the trigger efficiency and the geometrical acceptance:

$$\varepsilon_{\text{overall}} = \varepsilon_{\text{trigger}} \times \varepsilon_{\text{geom}} \tag{2}$$

where $\varepsilon_{\text{geom}}$ is the geometrical acceptance.

The geometric acceptance of the LHCb detector defines the spatial region and angular coverage within which decay products can be reliably detected and reconstructed. Only events whose final-state particles fall within this acceptance region are considered in the analysis. For example, to accurately reconstruct a Λ baryon decay, the decay vertex should lie within or close to the detector's acceptance, ensuring that its decay products traverse active detector regions. Consequently, the majority of Λ baryons produced in the simulation fall within this acceptance, and selection thresholds related to geometry have a minimal impact on their overall yield.

Two tracking configurations are considered in this study: LL and DD. The LL configuration refers to particles that are reconstructed using information from the VELO and all downstream tracking stations. It offers superior vertex resolution and momentum accuracy, making it more suitable for precise reconstruction of *b*-hadron decays. On the other hand, the DD configuration reconstructs particles that do not produce hits in the VELO but are still detectable in the downstream tracker. Although DD offers slightly better reconstruction efficiency due to its tolerance for highly displaced tracks, it lacks the resolution and precision of LL. Therefore, LL is preferred for rare decay studies where precise vertexing is essential [21]. A schematic diagram with the different tracks is given in Figure 6.

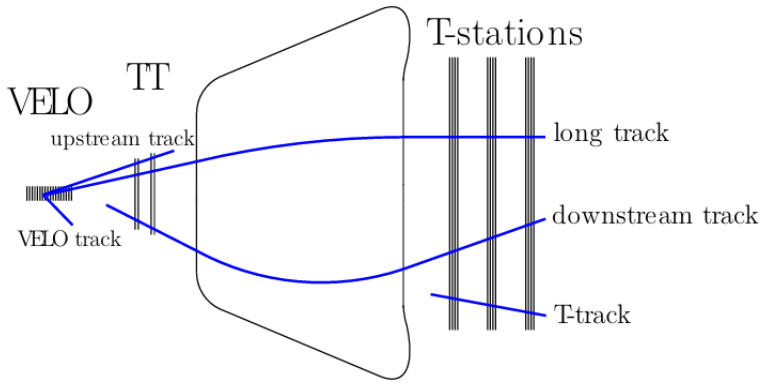

Figure 6: Sketch of the different types of tracks in LHCb: long, downstream, VELO, and upstream [24].

3.2 Simulation Environment

The simulation used in this analysis is RapidSim, a fast Monte Carlo generator designed to model the kinematic properties of heavy-flavour hadron decays. While RapidSim does not simulate detector response or low-level reconstruction effects, it is particularly useful for quickly generating large event

samples with realistic momentum distributions [11].

In this study, the decay $\Lambda_b \to \Lambda(\to p\pi^-)\mu^+\tau^-(\to \pi^-\pi^-\pi^+\nu_\tau)$, see Figure 7, is implemented explicitly, including all subdecays relevant to the kinematic structure. This approach allows the study of the complete topology of the final state while keeping the simulation lightweight. To simulate this decay, the dedicated trigger line `LbtoL0taumu_LambdaLLToPPi_TauTo3Pi` is used, which specifically targets this decay and its daughter particles.

Additionally, a background decay, $\Lambda_b \to \Lambda(\to p\pi^-)\tau^-(\to \pi^-\pi^-\pi^+\nu_\tau)\tau^+(\to \mu^+\bar{\nu}_\mu\nu_\tau)$, is also studied. This decay has a similar final-state topology to the signal decay but differs in that the muon originates from the τ^+ rather than directly from the Λ_b. Studying this background is important to understand potential contamination in the signal sample, as similar daughter particles and kinematics can affect reconstruction and selection. Since the daughters are the same, reconstruction can be performed similarly, but distinguishing between muons from direct decays and those from tau decays is crucial for accurate analysis.

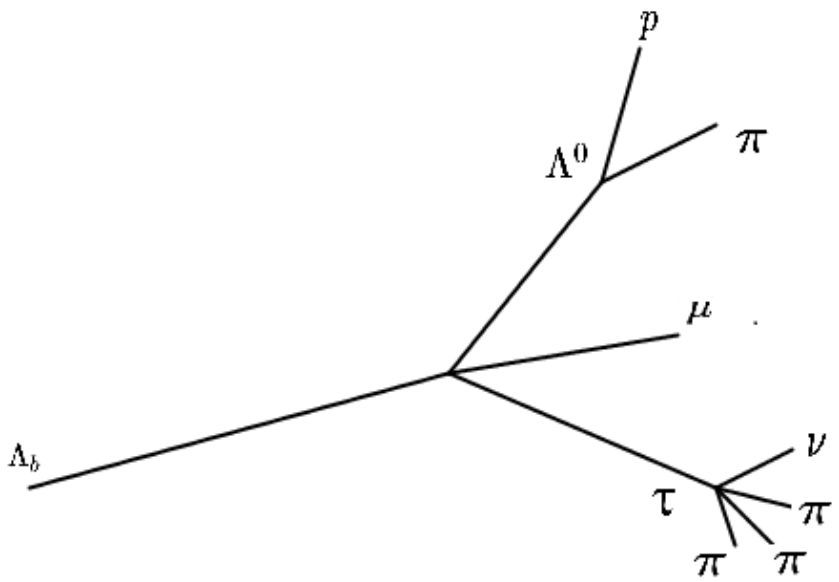

Figure 7: Diagram showing the full decay chain: $\Lambda_b \to \Lambda(\to p\pi^-)\mu^+\tau^-(\to \pi^-\pi^-\pi^+\nu_\tau)$.

In the study presented, the following two decay configurations are used: AllIn and AllDown. These represent simplified topologies replicating different tracking categories at LHCb. The AllIn setup corresponds to LL tracks, while the AllDown setup imitates DD tracks. Furthermore, neutrinos are marked as invisible in the configuration file, ensuring they are excluded from the final-state four-momentum sums. This reflects the physical reality that neutrinos are not detected and would otherwise bias the kinematic distributions used in trigger evaluation.

A total of 500,000 events were generated for each configuration to ensure statistical significance. Then, the number of selected events based on the configuration is recorded, and the simulation outputs are saved in ROOT format, which is then processed with a Python-based analysis. This code applies kinematic selection thresholds, as shown in Table 2, corresponding to the aforementioned trigger line, specificially, the mass, m, transverse momentum p_T, and momentum p since the simulation does not allow for the flight distance (FD) uncertainty, the impact parameter (IP), and the particle

identification (PID) to be recreated, reproducing a simplified hardware and software selection, rather than the full criteria used in LHCb Run 1 and Run 2. The resulting fraction of events passing the criteria is taken as the trigger efficiency as given in Equation 1.

Particles	$\mathbf{p_T}$**(GeV)**	**p(GeV)**	**m(GeV)**
Λ_b	1	3	2-10
Λ^0	0	0	$m_\Lambda - 1115.7 < 35$
τ	1	-	0.75 - 1.7
μ	0.5	3	-
p	0.25	2	-
π	0.25	2	-

Table 2: Selection thresholds on momentum (p), transverse momentum (p_T), and invariant mass (m) applied in the Python code to filter background data for the trigger line `LbtoL0taumu_LambdaLLToPPi_TauTo3Pi`, showing the respective thresholds for each final-state particle (p, π^-, μ, π^+) in both Long–Long (LL) and Down–Down (DD) categories.

Finally, two visualizations are produced: one shows trigger efficiency curves as a function of p_T for each final-state particle, proton, pion(s), muon, and the reconstructed Λ and τ. In these curves, the p_T threshold is varied for one particle at a time, while all other selection criteria remain fixed for the other particles. This isolates the effect of the p_T cut, which is important because transverse momentum strongly affects reconstruction efficiency, especially in hadron collider experiments like LHCb, where detector acceptance and trigger thresholds are typically defined in terms of p_T rather than total momentum or invariant mass. High p_T particles are more likely to be detected and reconstructed accurately due to their trajectories bending less in the magnetic field and producing clearer signals in the detectors. The other visualization is a bar chart summarizing the overall trigger efficiency for different trigger configurations. Together, these plots provide a clear picture of how trigger performance varies across particles and event topologies.

4 Results

To evaluate the trigger efficiency for the $\Lambda_b \to \Lambda \mu^{\pm} \tau^{\pm}$ decay, the selection thresholds in Table 2 are applied to the generated MC dataset. For each track configuration, the number of events passing the geometric acceptance and the selection thresholds is recorded. To study the impact of individual transverse momentum (p_T) cuts, efficiency curves are produced by varying the p_T threshold of one particle at a time, while keeping all other requirements fixed. This highlights the relative contribution of each particle to the total efficiency, with p_T being a key variable due to its influence on detector acceptance and reconstruction. A complementary filtering-flow chart shows how each selection step affects both the final trigger efficiency and the relative efficiency. The analysis is carried out separately for Long–Long (LL) and Downstream–Downstream (DD) reconstruction categories, each including opposite-sign charge combinations. A potential background process is also evaluated using the same selection scheme for comparison. Lastly, a detailed discussion of the plots and results is deferred to a later section.

4.1 $\Lambda_b \to \Lambda \tau^{\mp} \mu^{\pm}$

4.1.1 Long–Long Track Configuration

The first case considered is the decay $\Lambda_b \to \Lambda(\to p\pi^-)\mu^+\tau^-(\to \pi^-\pi^-\pi^+\nu_\tau)$ and its charge-conjugate $\Lambda_b \to \Lambda(\to p\pi^-)\mu^-\tau^+(\to \pi^-\pi^+\pi^+\bar{\nu}_\tau)$, restricted to the LL track configuration. Since the trigger system relies on the kinematic properties of the final-state particles, especially their transverse momentum and topology, it is important to evaluate how the decay structure influences geometric acceptance. Out of the 500,000 generated events, 145,554 are reconstructed in the LL geometry. This corresponds to a geometric LL acceptance of approximately $29.1 \pm 0.8\%$. From the selected events, the impact of transverse momentum cuts on the trigger efficiency of each decay product is shown in Figure 8.

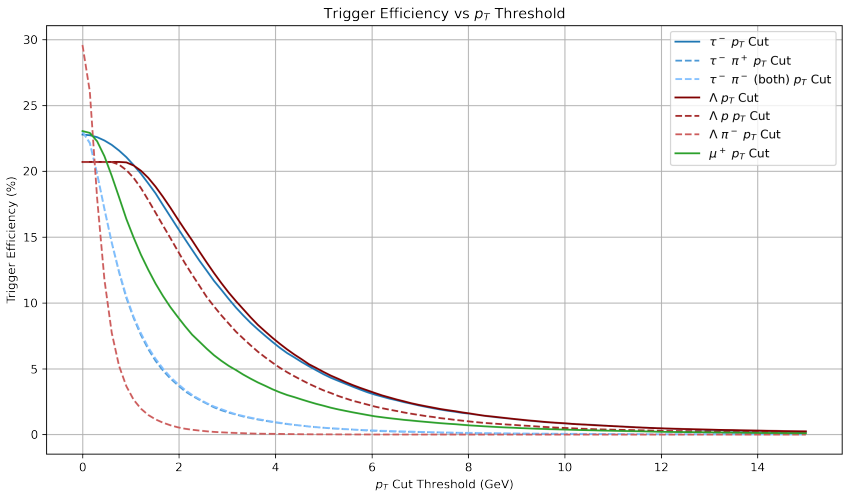

Figure 8: Plot showing the trigger efficiency ($\varepsilon_{trigger}$) as a function of the transverse momentum (p_T) for individual particles in the decay chain, including the initial particle, intermediate parents, and final-state daughters. The legend entries, read from left to right, indicate the parent particle, the corresponding daughter, and the variable being analyzed. This plot corresponds LL track configuration for the decay $\Lambda_b \to \Lambda(\to p\pi^-)\mu^+\tau^-(\to \pi^-\pi^-\pi^+\nu_\tau)$.

Furthermore, a cut-flow chart illustrating the effect of each sequential selection step on both the trigger efficiency and the relative efficiency is shown in Figure 9. Each ”Cut Stage” corresponds to the full set of selection criteria applied to a single particle. At each stage, only events that passed the

previous cuts are considered, so the filtering becomes progressively stricter as additional particles are included. The overall trigger efficiency, calculated using Equation 1, is found to be $20.7 \pm 0.8\%$ for the LL configuration.

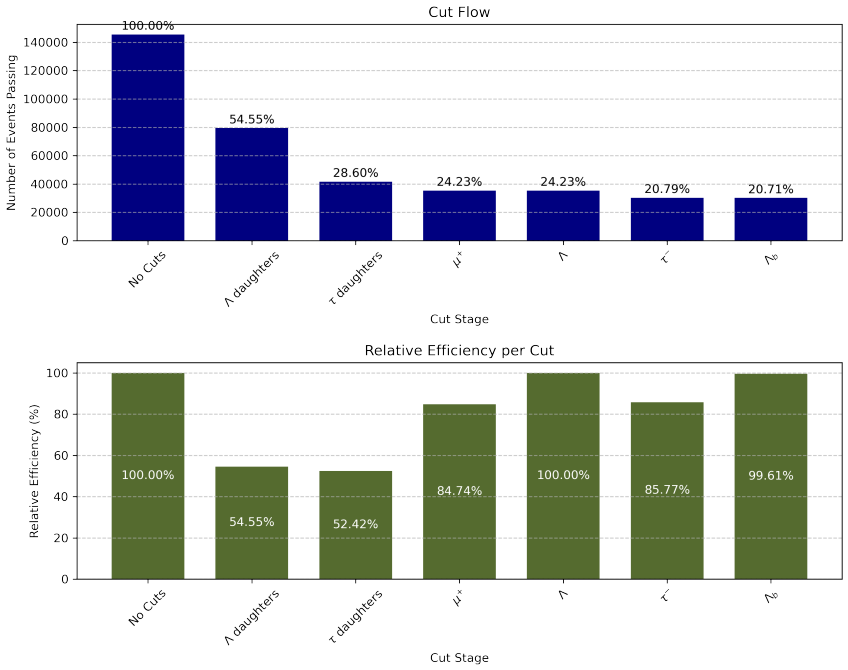

Figure 9: Bar chart showing the selection-flow for the LL configuration of the decay $\Lambda_b \to \Lambda(\to p\pi^-)\mu^+\tau^-(\to \pi^-\pi^-\pi^+\nu_\tau)$, illustrating the impact of each sequential selection step on the trigger efficiency and relative efficiency. Each stage applies the full set of selection criteria to one particle, and only events that passed the previous stages are retained.

The lepton charge-conjugate decay, $\Lambda_b \to \Lambda(\to p\pi^-)\mu^-\tau^+(\to \pi^-\pi^+\pi^+\bar{\nu}_\tau)$, corresponding to the same LL configuration as the previous case, yielded 145,727 selected events out of 500,000 generated. This corresponds to a geometric acceptance of $29.2 \pm 0.8\%$.

Similarly, the trigger efficiency as a function of transverse momentum cuts and the corresponding cut-flow chart are shown in Figure 10 and Figure 11, respectively. The trigger efficiency was found to be $20.5 \pm 0.8\%$. When combined with the geometrical acceptance, using Equation 2, the overall efficiency for both cases is found to be the same, $6.0 \pm 0.3\%$.

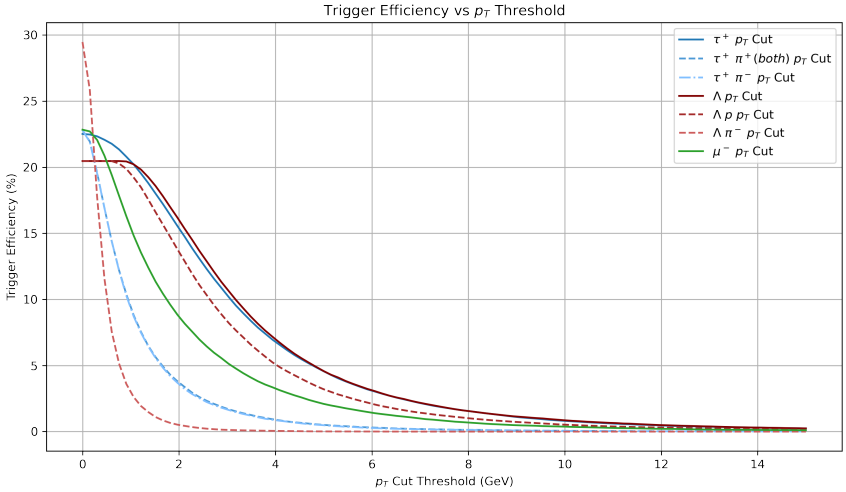

Figure 10: Plot showing the trigger efficiency ($\varepsilon_{trigger}$) as a function of the transverse momentum (p_T) for individual particles in the decay chain, including the initial particle, intermediate parents, and final-state daughters. The legend entries, read from left to right, indicate the parent particle, the corresponding daughter, and the variable being analyzed. This plot corresponds LL track configuration for the decay $\Lambda_b \to \Lambda(\to p\pi^-)\mu^-\tau^+(\to \pi^-\pi^+\pi^+\bar{\nu}_\tau)$.

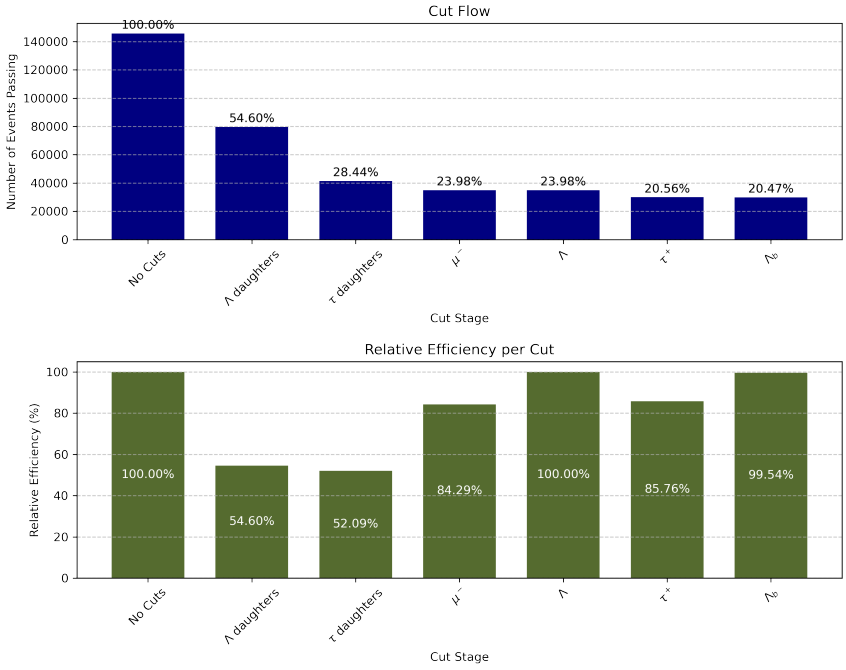

Figure 11: Bar chart showing the selection-flow for the LL configuration of the decay $\Lambda_b \to \Lambda(\to p\pi^-)\mu^-\tau^+(\to \pi^-\pi^+\pi^+\bar{\nu}_\tau)$, illustrating the impact of each sequential selection step on the trigger efficiency and relative efficiency. Each stage applies the full set of selection criteria to one particle, and only events that passed the previous stages are retained.

4.1.2 Downstream–Downstream Track Configuration

In this scenario, the acceptance is about $14.3 \pm 0.5\%$, since out of 500,000 events, only 71,718 are selected in the DD configuration. Therefore, the acceptance and resolution of DD is lower than in LL. Figure 12 and Figure 13 show the plot and the bar chart as in the LL configuration, respectively.

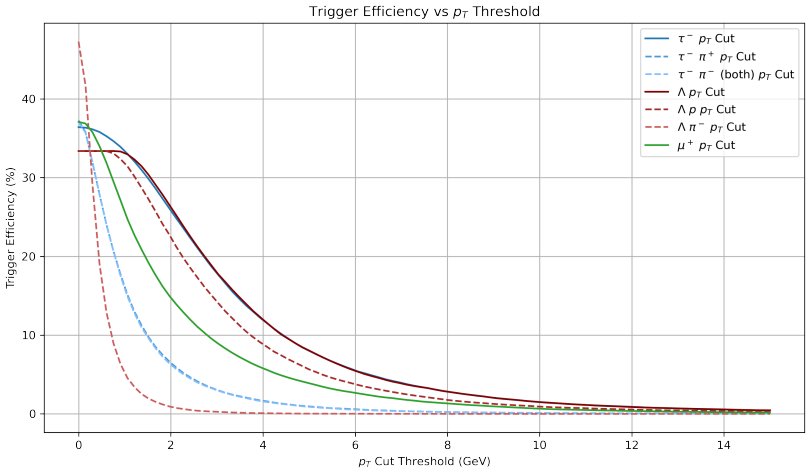

Figure 12: Plot showing the trigger efficiency ($\varepsilon_{trigger}$) as a function of the transverse momentum (p_T) for individual particles in the decay chain, including the initial particle, intermediate parents, and final-state daughters. The legend entries, read from left to right, indicate the parent particle, the corresponding daughter, and the variable being analyzed. This plot corresponds LL track configuration for the decay $\Lambda_b \to \Lambda(\to p\pi^-)\tau^+(\to \pi^+\pi^+\pi^-\bar{\nu}_\tau)\tau^-(\to \mu^-\nu_\mu\bar{\nu}_\tau)$.

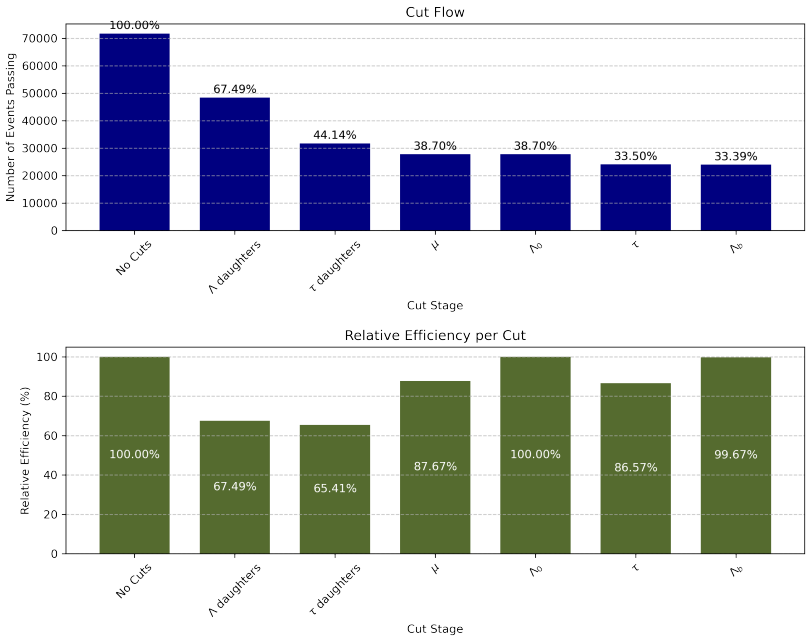

Figure 13: Bar chart showing the selection-flow for the LL configuration of the decay $\Lambda_b \to \Lambda(\to p\pi^-)\tau^+(\to \pi^+\pi^+\pi^-\bar{\nu}_\tau)\tau^-(\to \mu^-\nu_\mu\bar{\nu}_\tau)$, illustrating the impact of each sequential selection step on the trigger efficiency and relative efficiency. Each stage applies the full set of selection criteria to one particle, and only events that passed the previous stages are retained.

The final trigger efficiency was found to be $33.4 \pm 0.5\%$, which is higher than that observed in the LL category. Additionally, the conjugate decay is shown in Figure 14 and Figure 15 to increase the statistical significance. For the conjugate, the trigger efficiency was measured as $32.8 \pm 0.5\%$, and the geometric acceptance was $14.3 \pm 0.5\%$, based on 71,397 selected events out of 500,000. This results in an overall efficiency of $4.8 \pm 0.2\%$ for both decays.

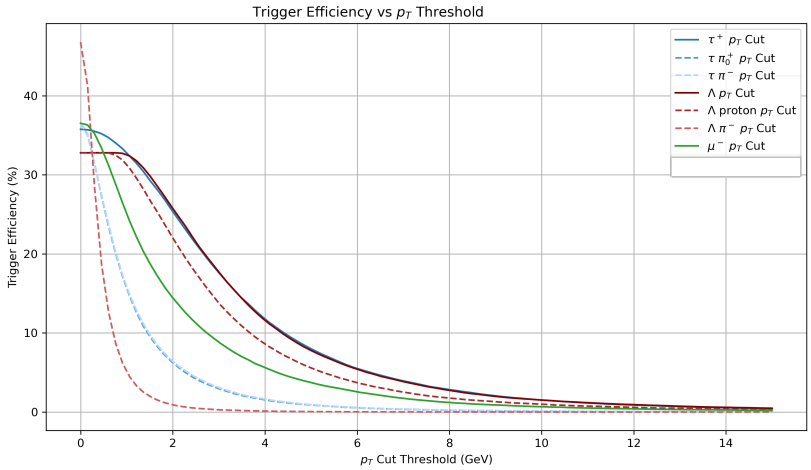

Figure 14: Plot showing the trigger efficiency ($\varepsilon_{trigger}$) as a function of the transverse momentum (p_T) for individual particles in the decay chain, including the initial particle, intermediate parents, and final-state daughters. The legend entries, read from left to right, indicate the parent particle, the corresponding daughter, and the variable being analyzed. This plot corresponds DD track configuration for the decay $\Lambda_b \to \Lambda(\to p\pi^-)\tau^+(\to \pi^+\pi^+\pi^-\bar{\nu}_\tau)\tau^-(\to \mu^-\nu_\mu\bar{\nu}_\tau)$.

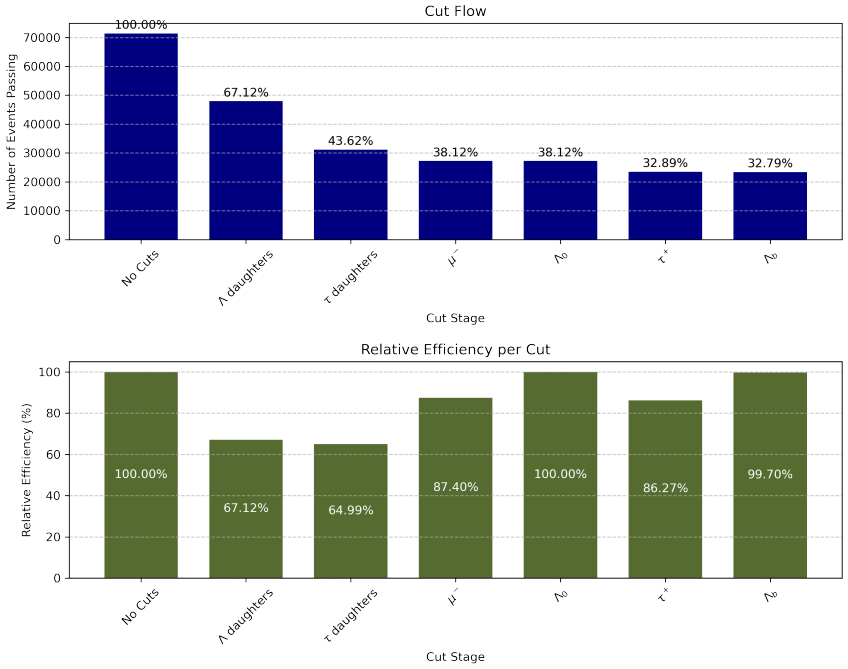

Figure 15: Bar chart showing the selection-flow for the DD configuration of the decay $\Lambda_b \to \Lambda(\to p\pi^-)\tau^+(\to \pi^+\pi^+\pi^-\bar{\nu}_\tau)\tau^-(\to \mu^-\nu_\mu\bar{\nu}_\tau)$, illustrating the impact of each sequential selection step on the trigger efficiency and relative efficiency. Each stage applies the full set of selection criteria to one particle, and only events that passed the previous stages are retained.

4.2 $\Lambda_b \to \Lambda\tau^\mp\tau^\pm$

4.2.1 Long–Long Track Configuration

To study a background decay similar to the signal channel, the decay $\Lambda_b \to \Lambda\tau^-\tau^+$ was investigated, including its charge-conjugate mode. In the LL track configuration, the number of selected events

was 152,254, as shown in Figure 16 and the corresponding selection-flow in Figure 17. The charge-conjugate decay is illustrated in Figure 18, with its selection-flow shown in Figure 19. For this sample, 153,085 events passed the selection. The geometric acceptance was measured as $30.5 \pm 0.8\%$ for the original decay and $30.6 \pm 0.8\%$ for the conjugate. The trigger efficiency was $13.7 \pm 0.8\%$ and $16.4 \pm 0.8\%$ for the original and conjugate modes, respectively.

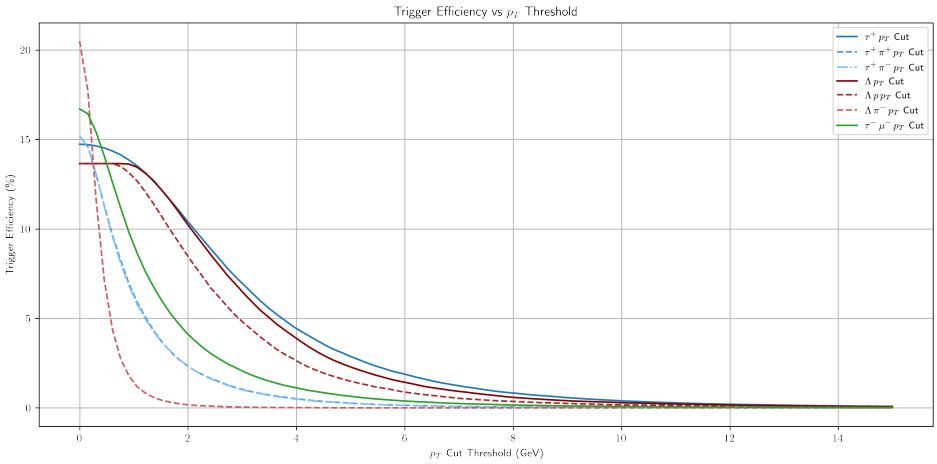

Figure 16: Plot showing the trigger efficiency ($\varepsilon_{trigger}$) as a function of the transverse momentum (p_T) for individual particles in the decay chain, including the initial particle, intermediate parents, and final-state daughters. The legend entries, read from left to right, indicate the parent particle, the corresponding daughter, and the variable being analyzed. This plot corresponds LL track configuration for the decay $\Lambda_b \to \Lambda(\to p\pi^-)\tau^-(\to \pi^-\pi^-\pi^+\nu_\tau)\tau^+(\to \mu^+\bar{\nu}_\mu\nu_\tau)$.

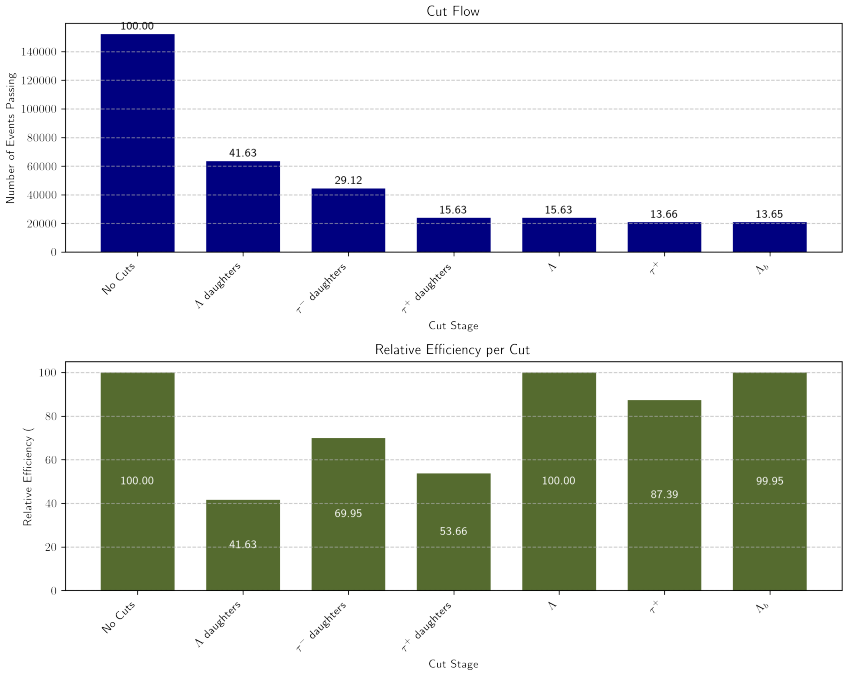

Figure 17: Bar chart showing the selection-flow for the LL configuration of the decay $\Lambda_b \to \Lambda(\to p\pi^-)\tau^-(\to \pi^-\pi^-\pi^+\nu_\tau)\tau^+(\to \mu^+\bar{\nu}_\mu\nu_\tau)$, illustrating the impact of each sequential selection step on the trigger efficiency and relative efficiency. Each stage applies the full set of selection criteria to one particle, and only events that passed the previous stages are retained.

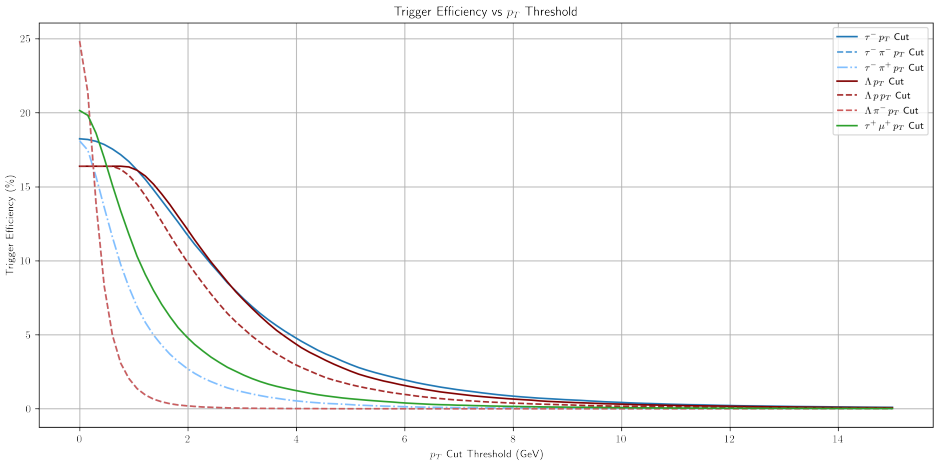

Figure 18: Plot showing the trigger efficiency ($\varepsilon_{trigger}$) as a function of the transverse momentum (p_T) for individual particles in the decay chain, including the initial particle, intermediate parents, and final-state daughters. The legend entries, read from left to right, indicate the parent particle, the corresponding daughter, and the variable being analyzed. This plot corresponds LL track configuration for the decay $\Lambda_b \to \Lambda(\to p\pi^-)\tau^+(\to \pi^+\pi^+\pi^-\bar{\nu}_\tau)\tau^-(\to \mu^-\nu_\mu\bar{\nu}_\tau)$.

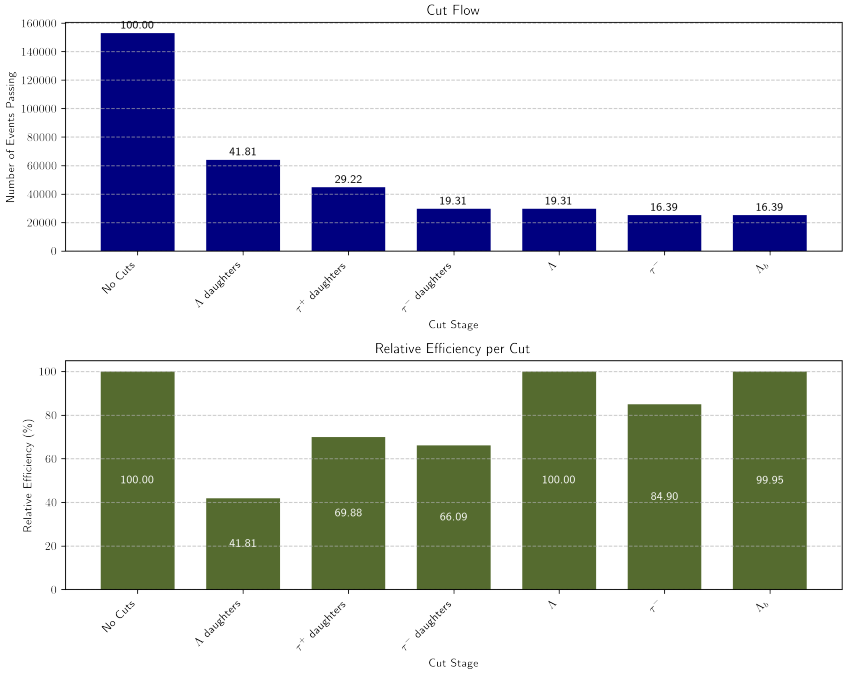

Figure 19: Bar chart showing the selection-flow for the LL configuration of the decay $\Lambda_b \to \Lambda(\to p\pi^-)\tau^+(\to \pi^+\pi^+\pi^-\bar{\nu}_\tau)\tau^-(\to \mu^-\nu_\mu\bar{\nu}_\tau)$, illustrating the impact of each sequential selection step on the trigger efficiency and relative efficiency. Each stage applies the full set of selection criteria to one particle, and only events that passed the previous stages are retained.

4.2.2 Downstream–Downstream Track Configuration

For the decay $\Lambda_b \to \Lambda\tau^-\tau^+$ in the DD configuration, a total of 66,262 events passed the geometric acceptance out of 500,000 generated events, resulting in a geometric acceptance of $13.3 \pm 0.5\%$. For the corresponding charge-conjugate decay, 66,931 events passed the same criteria, yielding a geometric acceptance of $13.4 \pm 0.5\%$. These results are shown in Figure 20, Figure 22, Figure 21,

and Figure 23. Furthermore, the trigger efficiency was found to be $25.2 \pm 0.5\%$ for the original decay mode and $28.3 \pm 0.5\%$ for the charge-conjugate mode.

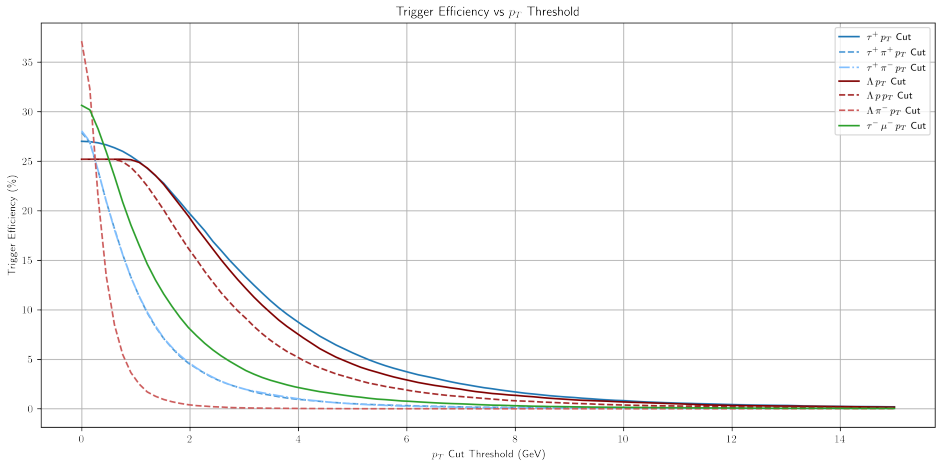

Figure 20: Plot showing the trigger efficiency ($\varepsilon_{trigger}$) as a function of the transverse momentum (p_T) for individual particles in the decay chain, including the initial particle, intermediate parents, and final-state daughters. The legend entries, read from left to right, indicate the parent particle, the corresponding daughter, and the variable being analyzed. This plot corresponds DD track configuration for the decay $\Lambda_b \to \Lambda(\to p\pi^-)\tau^-(\to \pi^-\pi^-\pi^+\nu_\tau)\tau^+(\to \mu^+\bar{\nu}_\mu\nu_\tau)$.

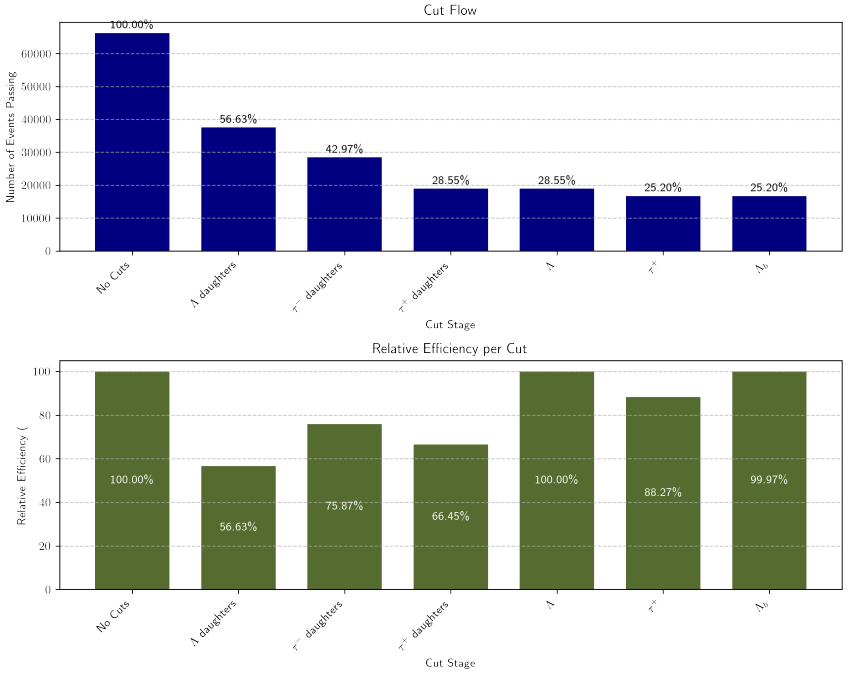

Figure 21: Bar chart showing the selection-flow for the DD configuration of the decay $\Lambda_b \to \Lambda(\to p\pi^-)\tau^-(\to \pi^-\pi^-\pi^+\nu_\tau)\tau^+(\to \mu^+\bar{\nu}_\mu\nu_\tau)$, illustrating the impact of each sequential selection step on the trigger efficiency and relative efficiency. Each stage applies the full set of selection criteria to one particle, and only events that passed the previous stages are retained.

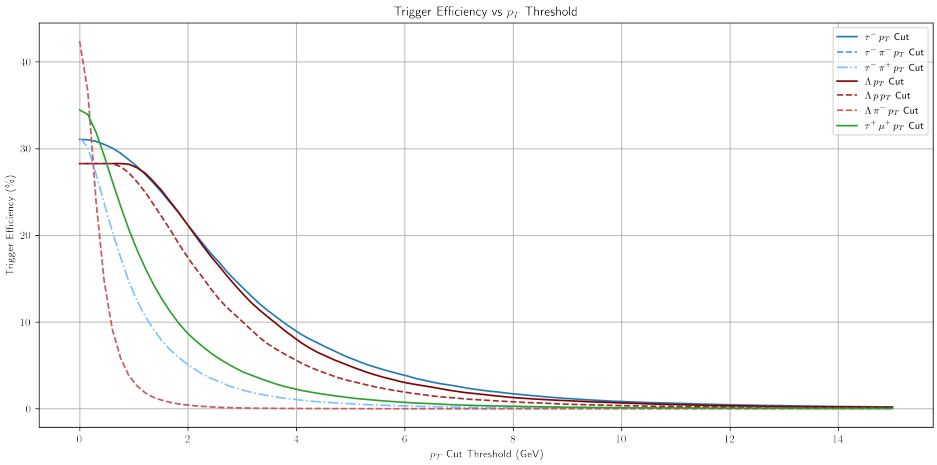

Figure 22: Plot showing the trigger efficiency ($\varepsilon_{trigger}$) as a function of the transverse momentum (p_T) for individual particles in the decay chain, including the initial particle, intermediate parents, and final-state daughters. The legend entries, read from left to right, indicate the parent particle, the corresponding daughter, and the variable being analyzed. This plot corresponds DD track configuration for the decay $\Lambda_b \to \Lambda(\to p\pi^-)\tau^+(\to \pi^+\pi^+\pi^-\bar{\nu}_\tau)\tau^-(\to \mu^-\nu_\mu\bar{\nu}_\tau)$.

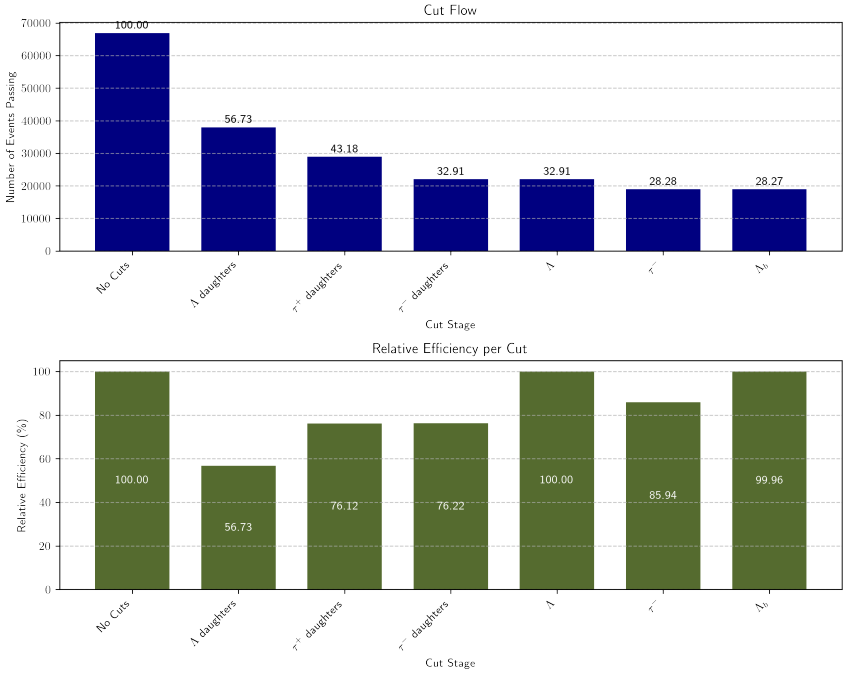

Figure 23: Bar chart showing the selection-flow for the DD configuration of the decay $\Lambda_b \to \Lambda(\to p\pi^-)\tau^+(\to \pi^+\pi^+\pi^-\bar{\nu}_\tau)\tau^-(\to \mu^-\nu_\mu\bar{\nu}_\tau)$, illustrating the impact of each sequential selection step on the trigger efficiency and relative efficiency. Each stage applies the full set of selection criteria to one particle, and only events that passed the previous stages are retained.

Table 3 shows the respective geometrical acceptance, trigger efficiency, and the product of both using Equation 2 for all the cases considered in this section.

Type of Decay	Geometrical Acceptance (%)	Trigger Efficiency (%)	Overall Efficiency (%)
$\Lambda_b \to \Lambda^0 \tau^- \mu^+$ (LL)	29.1 ± 0.8	20.7 ± 0.8	6.0 ± 0.3
$\Lambda_b \to \Lambda^0 \tau^+ \mu^-$ (LL)	29.2 ± 0.8	20.4 ± 0.8	6.0 ± 0.3
$\Lambda_b \to \Lambda^0 \tau^- \mu^+$ (DD)	14.3 ± 0.5	33.4 ± 0.5	4.8 ± 0.2
$\Lambda_b \to \Lambda^0 \tau^+ \mu^-$ (DD)	14.3 ± 0.5	32.8 ± 0.5	4.7 ± 0.2
$\Lambda_b \to \Lambda^0 \tau^+ \tau^-$ (LL)	30.5 ± 0.8	13.7 ± 0.8	4.2 ± 0.3
$\Lambda_b \to \Lambda^0 \tau^- \tau^+$ (LL)	30.6 ± 0.8	16.4 ± 0.8	5.0 ± 0.3
$\Lambda_b \to \Lambda^0 \tau^+ \tau^-$ (DD)	13.3 ± 0.5	25.2 ± 0.5	3.4 ± 0.1
$\Lambda_b \to \Lambda^0 \tau^- \tau^+$ (DD)	13.4 ± 0.5	28.3 ± 0.5	3.8 ± 0.2

Table 3: Geometrical acceptance, trigger efficiency, and overall efficiency (product of acceptance and trigger efficiency) for various Λ_b decay channels studied in this analysis. LL and DD refer to different track types.

5 Discussion

This discussion examines four distinct scenarios, as described in section 4, consisting of two LL and two DD configurations. Each configuration includes both the signal decay and a potential background decay, allowing for a comparative evaluation of trigger performance under different track-type topologies. The LL cases generally yield higher trigger efficiencies due to superior vertex resolution and tracking quality, while the DD configurations exhibit broader geometric acceptance. Including background decays in both LL and DD settings provides essential context for assessing the selectivity and effectiveness of the applied trigger conditions. The analysis that follows explores these trade-offs and highlights their impact on the trigger efficiency using the prexisting trigger lines.

In the first case for the LL topology, $\Lambda_b \to \Lambda(\to p\pi^-)\mu^+\tau^-(\to \pi^-\pi^-\pi^+\nu_\tau)$, the trigger efficiency as a function of transverse momentum (p_T), shown in Figure 8, reveals that the pion from the Λ decay achieves relatively high efficiency at low p_T values, indicating that most are produced with $p_T < 1\,\text{GeV}$, in line with expectations and corresponding to a geometric acceptance of approximately 30% in the absence of any p_T requirement. As the threshold increases, however, the efficiency declines sharply. The three pions from the τ decay exhibit similar behavior under p_T cuts, as they share identical kinematic constraints and overlapping p_T distributions due to originating from the same decay vertex. Despite all being pions, the Λ pion shows a steeper drop in efficiency, which can be attributed to the lower mass of the Λ compared to the τ, resulting in less available momentum for its decay products. Moreover, although the proton and pion from the Λ decay emerge with equal and opposite momenta in the Λ rest frame, this symmetry does not persist in the lab frame. Due to the typical forward boost of the Λ, the decay products undergo a Lorentz boost, during which the heavier proton inherits a greater share of the longitudinal momentum. This results in a harder p_T spectrum for the proton and a softer one for the pion, increasing the likelihood that the latter falls below the trigger threshold. Consequently, the current p_T cut at $0.25\,\text{GeV}$ for the pion is already near-optimal, as raising it further would cause a significant loss in trigger efficiency, as evident from the steep decline beyond this value in the daughter of Λ. Lowering it, however, would increase the trigger efficiency while simultaneously raising the rate of background events, potentially exceeding the bandwidth limitations of the data acquisition system or reducing the overall purity of the selected sample. Therefore, the threshold represents a trade-off between maximizing signal retention and maintaining manageable trigger rates.

Moreover, the trigger efficiency as a function of the proton p_T from the Λ decay declines more slowly than that of the other daughter particles, due to the proton's higher mass. Its behavior closely follows that of the Λ itself, suggesting that p_T selections applied to the proton act as effective safeguards, especially since the pion from the same decay shows a much sharper efficiency drop. However, beyond $1\,\text{GeV}$, the trigger efficiency for both the Λ and the proton begins to decline rapidly, with the proton being affected at a slightly lower p_T threshold. Additionally, the τ and μ particles initially exhibit higher trigger efficiencies than the Λ when no p_T cut is applied. The τ efficiency converges with that of the Λ soon after $1\,\text{GeV}$, while the μ efficiency drops more steeply, settling between the parent particles and their daughters, excluding the proton. This reflects the underlying mass difference between the leptons, as the heavier τ produces more energetic decay products, allowing stricter p_T thresholds to be applied without severely compromising efficiency.

Table 3 shows that reversing the charges of $\tau^\pm$ and $\mu^\pm$ has no significant effect on trigger selection efficiency for both signal and background decays. For the signal decay in the LL configuration, the rel-

ative difference in trigger efficiency is only 1.17%, with values of $20.7 \pm 0.8\%$ and $20.5 \pm 0.8\%$, likely due to statistical fluctuations and small differences in acceptance of $29.1 \pm 0.8\%$ and $29.2 \pm 0.8\%$, respectively. The overall efficiency (see Table 3) is effectively identical at $6.0 \pm 0.3\%$ for both charge configurations. The other charge conjugate cases exhibit similar behavior, with only slight variations in overall efficiency, trigger efficiency, and geometrical acceptance. This consistency aligns with the LHCb muon detector's known charge symmetry and the fact that hadronic τ decays depend primarily on mass, energy, and momentum rather than particle charge. The observed differences fall below the 1.2% threshold reported in previous LHCb performance studies [21]. Consequently, combining both charge configurations is justified, effectively doubling the data sample size and reducing statistical uncertainties.

The acceptance efficiency decreases from $29.1 \pm 0.8\%$ in LL to $14.3 \pm 0.5\%$ in DD, representing a 50% drop. This is primarily due to the DD configuration's shorter tracking region and reduced spatial resolution, which places vertices further downstream and makes precise reconstruction of short-lived particles more challenging. Consequently, events reconstructed in the LL configuration are unlikely to be reconstructed in DD, indicating that these two configurations are largely mutually exclusive. Despite this, the trigger efficiency per particle increases in DD, as shown in Figure 12, due to the trigger's enhanced ability to select events with longer flight paths and more displaced vertices. Overall, the DD trigger efficiency reaches $33.4 \pm 0.5\%$, a 63.12% increase over the LL value of $20.5 \pm 0.8\%$. While higher trigger efficiency is beneficial for detecting this rare decay, the significantly reduced acceptance in DD highlights an important trade-off between the two configurations.

Lastly, Figure 9 shows a selection-flow illustrating how each successive selection criterion reduces the sample size. The requirements applied to the π and p from Λ result in a relative efficiency decrease of 60%. Following the selection on the τ daughters, the three pions, another 50% of the sample is rejected. Subsequent selection criteria have a smaller impact on the sample size. Therefore, most particles are rejected during the initial reconstruction of the final-state products. Those passing these selections are further reduced by about 15% when applying the requirements related to the μ and τ. However, the subsequent requirements related to Λ and Λ_b properties do not lead to significant changes in the trigger efficiency. Although the order of the selection steps is important, it was chosen based on the reconstruction logic, starting from the final products and working backward to the parent particles. This is attributed to the acceptance geometry, which ensures that the Λ decay vertices lie within the detector coverage, rendering the applied criteria ineffective in further reducing these candidates. For the DD configuration, depicted in Figure 13, the reconstruction efficiency is higher due to the highly displaced daughters, which may escape the VELO but still be detected in the downstream tracker. Nevertheless, for most Λ_b decays, LL tracks are preferred because of their higher momentum resolution and precise vertexing, which are crucial for identifying b-hadron decays.

The efficiencies given in Table 3 indicate relatively limited sensitivity for this decay, despite the use of existing LFV trigger lines. These triggers are not as optimized as the dedicated lines developed for well-studied rare decays such as $B \to \mu\mu$, which require very high efficiencies due to their extremely small branching ratios. While $B \to \mu\mu$ benefits from highly specialized triggers that maximize signal retention, the current LFV triggers for $\Lambda_b \to \Lambda\tau\mu$ offer lower efficiency, limiting the number of signal events collected and thus reducing experimental sensitivity. Implementing new dedicated trigger lines could improve signal acceptance and increase the overall sensitivity of the experiment for these rare events. However, their design is complicated by the final-state topology involving displaced vertices and neutrinos from τ decay that cause missing momentum and make reconstruction challenging. Fur-

thermore, adding dedicated triggers must balance gains in efficiency with increased trigger rates and resource demands, highlighting an important trade-off in trigger strategy.

Furthermore, the use of RapidSim, a fast MC generator relying mainly on basic kinematic properties, also affects the precision and uncertainty of the trigger efficiency values. Since RapidSim does not simulate detailed detector effects like particle identification (PID), impact parameter, or flight distance uncertainties, these parameters had to be excluded from the trigger line analysis, even though they are used in the actual LHCb trigger lines. In real trigger lines, these variables help to distinguish signal from background. Although no background was generated in this simulation, the absence of these variables reduces the trigger's effectiveness. Because of this, the estimated trigger efficiency is likely higher than what would be observed in reality. As such, using a more complete simulation chain, combining Gauss (event generation), Boole (detector simulation), and Brunel (event reconstruction), would produce detailed information that Moore can process for accurate trigger studies. However, such full simulations require significantly more computing power, especially when including realistic background events and detector conditions. Therefore, RapidSim can be used for fast approximations, but more detailed simulations are needed to provide additional relevant information for accurate trigger studies.

6 Conclusion

The thesis aimed to simulate the rare decay $\Lambda_b \to \Lambda\mu^{\pm}\tau^{\mp}$ to evaluate the efficiency of existing trigger lines in selecting this event, a decay forbidden in the SM due to LFV, and thus a promising window onto physics BSM. In addition, the background decay $\Lambda_b \to \Lambda\tau^{\pm}\tau^{\mp}$, which shares the same final-state topology, was investigated to provide a comparative baseline. This was achieved by applying a set of kinematic selection criteria currently implemented in the LHCb trigger system. Furthermore, individual transverse momentum (p_T) thresholds for each particle were studied by varying the p_T of one particle at a time and comparing the resulting efficiencies. A selection-flow analysis was then performed to quantify how each particle selection influenced the overall trigger efficiency, highlighting specific parameters that may benefit from further optimization. Lastly, the inclusion of the background decay enabled a direct comparison to better understand the trigger performance.

It was found that the largest impact on trigger efficiency was due to the pions, specifically the pions from Λ. When no p_T selection was applied to the pion, the efficiency was highest, around 30%. However, after applying a transverse momentum (p_T) cut of 0.25 GeV, the efficiency rapidly decreased, and beyond 1 GeV it plateaued and became flat. This indicates that most of the pion daughters of Λ lie within the provided threshold range. Decreasing the p_T selection further would risk increasing background contamination. Similarly, the pion daughters from τ show a comparable trend due to momentum being shared among the three decay products, but differ from the Λ pions because of the difference in mass between their parent particles. On the other hand, the proton daughters from Λ had less impact on the trigger efficiency compared to the pions, largely because the proton, being heavier, generally carries higher transverse momentum after the decay and Lorentz boost. This results in the proton more often passing the p_T thresholds used in the trigger, while the lighter pions frequently fall near or below these selections, making the trigger efficiency more sensitive to pion selection criteria. Consequently, the p_T filters for pions cannot be optimized further without a significant loss.

The parent particles exhibited more stable behavior compared to their daughters, primarily because the daughters' kinematic selections had already restricted the trigger efficiency. This reduced the need for imposing stricter cuts on the parent particles. The τ showed a higher trigger efficiency than the Λ, with its efficiency converging to that of the Λ line after a transverse momentum cut of 1 GeV. The μ was found to lie between the Λ and τ in terms of efficiency, despite starting with the same trigger efficiency as the τ. The τ daughters exhibited trigger efficiencies similar to those of the τ at low p_T values. Consequently, only the μ selection criteria could be tightened without causing a significant loss in efficiency. Therefore, optimizing the μ cuts offered the most potential for improving trigger performance without significant efficiency loss.

Lastly, as shown in Table 3, the DD configuration demonstrated better trigger efficiency than LL, despite having lower spatial precision. This increased efficiency stems primarily from the fact that DD tracks do not require hits in the VELO, allowing acceptance of tracks that bypass the vertex locator entirely. Such a feature benefits highly displaced decays, including those involving long-lived particles. However, this advantage comes at the cost of reduced vertex resolution, which is essential for accurate reconstruction of b-hadrons. Consequently, although DD provides higher efficiency in certain cases, LL remains the preferred configuration due to its superior spatial resolution and reconstruction capabilities. Combining both LL and DD tracks, however, improves overall decay reconstruction by increasing the number of considered signal events. Despite these improvements, the overall efficiency remained below 10% in all cases, emphasizing the importance of improving both detector acceptance

and trigger selections to enhance signal sensitivity.

This study relied on RapidSim, a fast MC generator that simulates basic kinematic properties, which inherently limits the precision and statistical accuracy of the estimated trigger efficiencies. Since RapidSim does not incorporate detailed detector effects such as PID, IP, or FD uncertainties, the variables had to be excluded from the analysis, likely resulting in an overestimation of the trigger efficiency compared to what would be observed with full detector simulation. Moreover, no background events were included in the simulation, further limiting the realism of the efficiency estimate. To improve the accuracy and reliability of trigger efficiency studies, future work should incorporate the full LHCb simulation chain, Gauss for event generation, Boole for detector simulation, and Brunel for event reconstruction, despite the substantially increased computational resources required. This would enable a more realistic evaluation of trigger performance, including the effects of some background and detector conditions.

Furthermore, the existing LFV trigger lines used for the rare decay $\Lambda_b \to \Lambda \tau \mu$ exhibit relatively low overall efficiency, as shown in Table 3. The trigger efficiency is within acceptable ranges for the LL category, as expected, but suffers from low efficiency in the DD category. This limitation reduces the number of signal events collected and consequently decreases the experimental sensitivity. Since these triggers are not as finely optimized as those designed for well-studied rare decays such as $B \to \mu\mu$, designing dedicated trigger lines could improve signal acceptance and increase sensitivity. Additionally, optimizing trigger parameters related to the muon and lowering the pion transverse momentum threshold could significantly enhance the trigger efficiency. However, the complex final-state topology poses significant challenges: displaced vertices and neutrinos from the τ decay result in missing momentum, complicating both event reconstruction and trigger decision-making. Moreover, any increase in trigger efficiency achieved by adding dedicated lines must be carefully balanced against the resulting increases in trigger rates and resource demands, highlighting an essential trade-off in trigger strategy development.

In conclusion, the trigger efficiencies obtained for both the LL and DD configurations demonstrate that while current LFV trigger lines provide a baseline level of sensitivity, there remains significant room for improvement. For the signal decay $\Lambda_b \to \Lambda \tau \mu$, the LL configuration achieved efficiencies of $20.7 \pm 0.8\%$, compared to $13.7 \pm 0.8\%$ for the background decay. In the DD configuration, the signal efficiency reached about $33.4 \pm 0.5\%$, while the background remained at $25.2 \pm 0.5\%$. Despite these relatively high individual component efficiencies, the overall efficiency for reconstructing the full decay chain remained low, fluctuating between $3.4 \pm 0.1\%$ and $6 \pm 0.3\%$. These values highlight the need for more tailored trigger strategies. Developing dedicated trigger lines specifically tailored to the $\Lambda_b \to \Lambda \tau \mu$ decay, along with careful optimization of particle selection thresholds, particularly for the muon and pion, could substantially enhance signal acceptance and overall experimental sensitivity. However, such improvements must be balanced with practical considerations such as increased trigger rates and available computational resources. Future studies incorporating full detector simulations and realistic background conditions will be crucial to accurately assess these optimizations and guide the design of more efficient trigger strategies for rare decay searches at LHCb.

Bibliography

[1] LHCb collaboration, R. Aaij *et al.*, *First Evidence for Direct CP Violation in Beauty to Charmonium Decays*, Phys. Rev. Lett. **134** (2025) 101801, arXiv:2411.12178.

[2] G. Pathak and M. K. Das, *Matter-antimatter asymmetry in minimal inverse seesaw framework with A_4 modular symmetry*, arXiv:2505.03000.

[3] H. Nunokawa, S. Parke, and J. W. F. Valle, *CP violation and neutrino oscillations*, Progress in Particle and Nuclear Physics **60** (2008) 338–402.

[4] LHCb collaboration, R. Aaij *et al.*, *Observation of charge-parity symmetry breaking in baryon decays*, arXiv:2503.16954.

[5] S. Biswas, P. Nayek, P. Maji, and S. Sahoo, *Lepton flavour violating Λ_b decays in non-universal Z' model*, Eur. Phys. J. C **81** (2021) 493, arXiv:2310.11314.

[6] M. Bordone, M. Rahimi, and K. K. Vos, *Lepton flavour violation in rare Λ_b decays*, Eur. Phys. J. C **81** (2021) 756, arXiv:2106.05192.

[7] LHCb collaboration, R. Aaij *et al.*, *Search for the decays $B_s^0 \to \tau^+\tau^-$ and $B^0 \to \tau^+\tau^-$*, Phys. Rev. Lett. **118** (2017) 251802, arXiv:1703.02508.

[8] A. Pich, *Lessons learnt from the heavy tau lepton*, 2000. Available at: https://cerncourier.com/a/lessons-learnt-from-the-heavy-tau-lepton/ (Accessed on 12/06/2025).

[9] LHCb collaboration, S. Celani, *Lepton Flavour Universality tests and Lepton Flavour Violation searches at LHCb*, in *16th International Workshop on Tau Lepton Physics* , 2021, arXiv:2111.11105.

[10] J. Closier, *Muon system*, 2021. Available at: https://lhcb-outreach.web.cern.ch/detector/muon-system-2/ (Accessed on 12/06/2025).

[11] G. A. Cowan, D. C. Craik, and M. D. Needham, *RapidSim: An application for the fast simulation of heavy-quark hadron decays*, Computer Physics Communications **214** (2017) 239–246.

[12] ATLAS collaboration, G. Aad *et al.*, *A detailed map of Higgs boson interactions by the ATLAS experiment ten years after the discovery*, Nature **607** (2022) 52, arXiv:2207.00092, [Erratum: Nature 612, E24 (2022)].

[13] D. J. Griffiths, *Introduction to Elementary Particles*, Wiley-VCH, 2nd revised edition ed., 2008.

[14] Wikipedia contributors; Cush, *File:standard model of elementary particles.svg*, 2019. Accessed: 2025-06-19.

[15] A. de Gouvêa and P. Vogel, *Lepton flavor and number conservation, and physics beyond the standard model*, Progress in Particle and Nuclear Physics **71** (2013) 75–92.

[16] S. Lavignac, *Flavor and CP violation in the lepton sector and new physics*, eConf **C030603** (2003) VEN04, arXiv:hep-ph/0312309.

[17] C.-X. Yue and J.-R. Zhou, *New gauge boson $Z^{'}$ and lepton flavor violating decays and production of vector mesons*, Phys. Rev. D **93** (2016) 035021.

[18] L. Greeven, *Decoding beauty: rare baryonic decays SciFi detector commissioning*, PhD thesis, Maastricht University, Netherlands, 2024, doi: 10.26481/dis.20240403lg.

[19] M. Bordone, M. Rahimi, and K. K. Vos, *Lepton flavour violation in rare Λ_b decays*, Eur. Phys. J. C **81** (2021) 756, arXiv:2106.05192.

[20] S. Navas and others (Particle Data Group), *Review of particle physics*, Physical Review D **110** (2024) .

[21] LHCb collaboration, R. Aaij *et al.*, *LHCb Detector Performance*, Int. J. Mod. Phys. A **30** (2015) 1530022, arXiv:1412.6352.

[22] Nikhef, *LHCB*, Available at: https://www.nikhef.nl/en/programs/lhcb/ (Accessed on 12/06/2025).

[23] LHCb collaboration, The LHCb Collaboration et al, *The LHCb Detector at the LHC*, JINST **3** (2008) S08005.

[24] LHCb collaboration, R. Aaij *et al.*, *Design and performance of the LHCb trigger and full real-time reconstruction in Run 2 of the LHC*, JINST **14** (2019) P04013, arXiv:1812.10790.

[25] LHCb collaboration, The LHCb Collaboration et al, *The LHCb Upgrade I*, JINST **19** (2024) P05065, arXiv:2305.10515.